Dalton Transactions

PAPER

View Article Online
View Journal | View Issue

Cite this: *Dalton Trans.*, 2026, **55**, 6863

Electronic effects of *para*-phenolate substitution in an extended series of neutral and oxidized chromium salen nitrides

Warren VandeVen,[a] Samyadeb Mahato,[a] Avery LeComte,[a] Gregory A. MacNeil,[a] Wen Zhou,[a] Fabrice Thomas,[b] Charles J. Walsby,[a] Mario U. Delgado-Jaime[c] and Tim Storr*[a]

High-valent transition-metal nitrides have recently emerged as versatile platforms for N-atom transfer, and their reactivity remains sensitive to subtle electronic perturbations. Cr salen (where "salen" represents N_2O_2 bis-phenolate bis-Schiff-base ligands) nitrides offer a rare platform in which both the metal center and the redox-active salen ligand are both susceptible to one-electron oxidation, enabling systematic evaluation of how salen ligand substituent effects can change the electronic structure, and ultimately nitride reactivity. Herein, we evaluate a series of **CrNSal^{R}** complexes to better understand how changing the ancillary ligand donating ability *via* the *para*-phenolate substituent (R = NO_2, CF_3, H, *t*Bu, OMe, O*i*Pr, NMe_2) dictates overall electronic structure. For electron-donating R = OMe and R = OiPr, designed to probe the threshold for switching the oxidation locus from metal to ligand, one-electron oxidation results in a metal-centered Cr(VI) nitride, extending the window for metal-based oxidation beyond the previously established R = *t*Bu derivative. In contrast, the R = NO_2-substituted analogue, while not promoting bimolecular nitride coupling as observed in Mn congeners, nonetheless renders the Cr≡N unit more electrophilic than previously reported R = CF_3-substituted systems. Together, these results expand the electronic landscape of Cr-salen-nitrides and demonstrate how fine-tuning the donating ability of the ancillary salen ligand can be used to systematically manipulate the electronic structure at the nitride.

Received 17th October 2025,
Accepted 23rd March 2026

DOI: 10.1039/d5dt02506k

rsc.li/dalton

1. Introduction

High-valent transition-metal nitrides have garnered significant interest as versatile reagents in stoichiometric and catalytic N-atom transfer, a reactivity space that, unlike their oxo counterparts, remains comparatively underdeveloped.[1–7] The reactivity of high valent metal nitrides is governed by a number of parameters, including metal identity, oxidation state, coordination geometry, and ancillary ligand electronics.[8–11] From a molecular orbital perspective, electrophilic reactivity is typically associated with population of M≡N π* antibonding orbitals,[12–19] whereas nucleophilic pathways arise from filled M≡N π orbitals or the nitride lone pair.[20–23] Importantly, several discrete metal nitride complexes have demonstrated ambiphilic reactivity, underscoring how subtle changes in electronic structure can invert reactivity profiles.[24–28] Beyond their intrinsic synthetic value, nitrides have been used to understand the hydrogen atom bond dissociation free energy of associated imido complexes,[29] as key intermediates in ammonia oxidation,[30–32] and proton-coupled electron transfer pathways leading to ammonia production.[33–35] In this broader context, discrete and tunable transition metal nitrides serve as powerful models for mapping how local electronic structure dictates nitride reactivity.

Similarly to their Mn congeners, Cr salen complexes have been widely applied in catalysis, including olefin epoxidation,[36] copolymerization,[37] and oxidative cross-coupling,[38] underscoring the versatility of the salen platform. Stable Cr(V) and Cr(VI) nitrides supported by salen ligands are now well documented, with the former generally exhibiting nucleophilic character.[39–44] Additionally, high-valent Cr salen nitrides are markedly more stable than their Mn counterparts, as Mn nitrides are used as nitrogen atom transfer agents in preparation of Cr nitrides.[39,43,45] The stability of the Cr analogues provides a unique opportunity to interrogate how subtle perturbations to the electronic structure, particularly the locus of oxidation between metal and ligand, govern the reactivity of high-valent nitrides.

[a]*Department of Chemistry, Simon Fraser University, Burnaby, British Columbia, V5A 1S6, Canada. E-mail: tim_storr@sfu.ca*
[b]*Univ. Grenoble Alpes, CNRS, DCM, F-38000 Grenoble, France*
[c]*Department of Chemistry, University of Guadalajara, Guadalajara, Jalisco 44430, Mexico*

Our previous studies established that mono-oxidation of **CrNSal^{R}** complexes can be either metal- or ligand-centered depending on the *para* substituent (R).[24] Electron-withdrawing substituents such as CF_3 (σ_p = +0.54) and moderately donating *t*Bu (σ_p = −0.20) result in metal-based oxidation to generate Cr(VI), yielding electrophilic nitrides, whereas strongly donating NMe_2 (σ_p = −0.83) resulted in ligand-based oxidation, affording Cr(V)–ligand radical species that retain nucleophilic character at the nitride.[24,46] This divergence in oxidation locus directly translates into distinct nitride reactivity profiles, highlighting the potential to tune electrophilic *vs.* nucleophilic N-atom transfer by modulating ligand electronics. On this basis, we hypothesized that within the Hammett window defined by *t*Bu and NMe_2 ($-0.20 < \sigma_p > -0.83$),[46] there may exist *para*-ring substituents capable of supporting valence tautomerism,[47–52] which in other systems has been shown *via* temperature modulation and exogenous donor coordination. Accordingly, R = OMe (σ_p = −0.27) and R = O*i*Pr (σ_p = −0.45) substituents were targeted to probe this threshold region where the oxidation locus is predicted to switch. In parallel, a strongly electron-withdrawing derivative, R = NO_2 (σ_p = +0.78), was synthesized to test whether increase electron-withdrawing R-groups could promote bimolecular nitride coupling,[11,29,32,53] a facile reaction pathway for **[Mn^{VI}NSal^{CF3}]$^{+}$** but much slower for the Cr analogue. Finally, the unsubstituted parent (R = H) was included to complete the series and provide a reference point for future Hammett-based reactivity correlations. This expanded **CrNSal^{R}** series thus enables a systematic interrogation of how incremental electronic perturbations, that are remote to the metal coordination site, govern oxidation locus and, by extension, nitride reactivity (Scheme 1).

2. Results and discussion

2.1. Synthesis

Salen ligands were prepared by condensing two equiv. of substituted 3-*tert*-butyl-2-hydroxybenzaldehydes with one equiv. of (±)-*trans*-1,2-diaminocyclohexane, following literature procedures.[11,17,53] Substituents were selected to expand the range of Hammett σ_p values and systematically probe electronic effects on structure and reactivity. Two general synthetic strategies were employed to access the **CrNSal^{R}** complexes. Both methods utilize **MnNSal^{H}** as a nitride donor, leveraging the thermodynamic favourability of nitride transfer and the low solubility of the **MnClSal^{H}** byproduct to simplify purification. In the first approach, $CrCl_3$·3THF was treated with MnNSal^{H} to generate a reactive $[CrN]^{2+}$ intermediate that was subsequently ligated with **H$_2$Sal^{R}** (Scheme 2A).[45] In the second approach, **CrClSal^{H}** was prepared and reacted with **MnNSal^{H}** following a protocol developed by Neely and Bottomley (Scheme 2B).[54] The first route was required for R = NO_2 and H due to the poor solubility of the corresponding **CrClSal^{R}** intermediates. Where feasible, products were purified by silica gel chromatography. All complexes were characterized by ESI-MS and elemental analysis and are consistent with the proposed formulations. Additionally, Evans method NMR confirmed the presence of a single unpaired electron per complex, in line with a Cr(V), d^1 configuration. We have recently reported limited characterization and reactivity data for the O*i*Pr derivative,[24] and in the present work, we report the full synthesis, comprehensive spectroscopic characterization, and detailed electronic-structure analysis of the **CrNSal^{OiPr}** derivative.

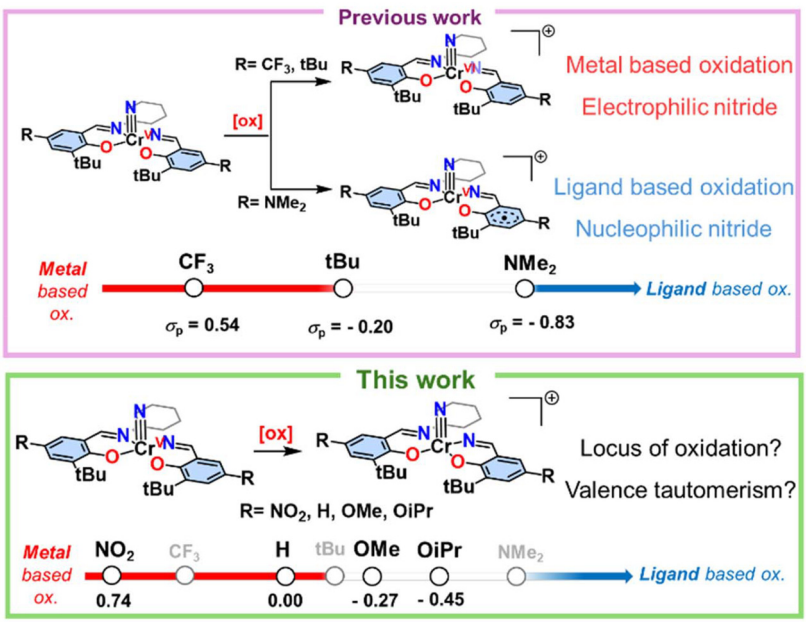

Scheme 1 Electronic effects of *para*-phenolate substitution in an extended series of neutral and oxidized chromium salen nitrides.

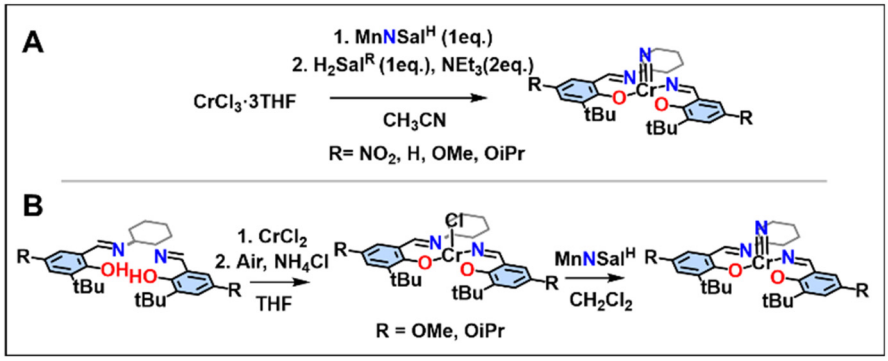

Scheme 2 Synthetic routes to target **CrNSal^{R}** complexes. Either a $[CrN]^{2+}$ fragment can be generated *in situ* and reacted with substituted salen ligand (A), or the **CrClSal^{R}** intermediate can be synthesized and reacted with the nitride transfer reagent (B).

2.2. Solid state structures

Crystals suitable for single-crystal X-ray diffraction (SC-XRD) were obtained by slow evaporation or solvent layering techniques using appropriate solvent systems (Fig. 1). **CrNSal^{OiPr}** was crystallized by layering hexane over THF, while **CrNSal^{OMe}** formed crystals upon slow evaporation from hot CH_3CN. Crystals of **CrNSal^{NO2}** and **CrNSal^{H}** were obtained by layering CH_3CN over CH_2Cl_2 solutions. X-ray crystallographic analysis of **CrNSal^{R}** complexes (R = NO_2, H, OMe, O*i*Pr) confirms the expected distorted square pyramidal geometry with the nitrido ligand occupying the apical position and the Cr center situated approximately 0.50 Å above the mean plane defined by the four salen donor atoms (Fig. 1 and Table S2). The most significant distortion is observed for **CrNSal^{H}**. The Cr≡N bond lengths are 1.560(4) Å for R = NO_2, 1.549(2) Å for R = H, 1.556 (5) Å for R = OMe, and 1.538(1) Å for R = O*i*Pr. These short distances are indicative of strong Cr≡N triple bond character and closely match those reported for **CrNSal^{tBu}** at 1.553(3) Å, **CrNSal^{NMe2}** at 1.546(7) Å, and other structurally characterized Cr(v) nitride species.[24,39,40] Additionally, the Cr–N_{salen} (1.944 (1)–1.966(2) Å), Cr–O_{salen} (1.878(2)–1.899(2) Å) distances, as well as the N–Cr–N and O–Cr–O angles, show minimal variation across the series reaffirming that *para*-substitution does not significantly perturb the geometry at the metal center (Table S2).

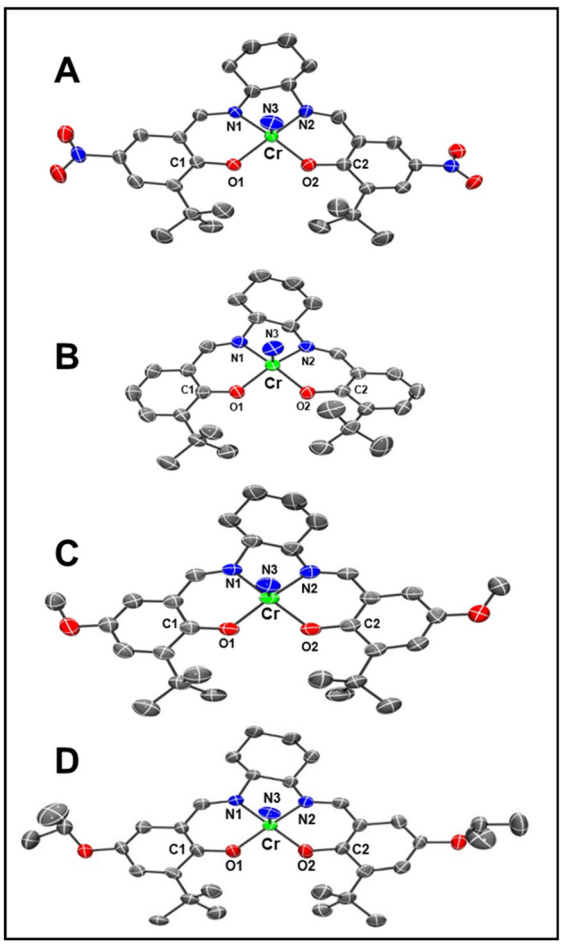

Fig. 1 POV-ray representation of **CrNSal^{R}** with R = NO_2 (A), H (B), OMe (C), and O*i*Pr (D). Thermal ellipsoids shown at 50% probability; H atoms and counteranions omitted for clarity (Cr, green; O, red; N, blue; C, grey). Selected bond lengths (Å): (A) Cr–N(3) = 1.560(4); (B) Cr–N(3) = 1.549(2); (C) Cr–N(3) = 1.556(5); (D) Cr–N(3) = 1.538(1) (see Tables S1 and S2 for more details).

2.3. Electrochemistry

Cyclic voltammetry (CV) experiments on four **CrNSal^{R}** derivatives (R = NO_2, H, OMe, OiPr) revealed a quasi-reversible oxidation process tunable by nearly 1 V, underscoring the strong influence of *para*-substitution on the redox properties of these Cr(v)-nitrides (Fig. 2, Table 1 and Fig. S1, S2). **CrNSal^{NO2}** exhibits a single redox process at $E_{1/2}$ = 0.91 V, consistent with the strongly electron-withdrawing nature of the R = NO_2 substituent (Fig. 2A). Notably, it is the only complex to display a reduction wave within the accessible electrochemical window, observed at *ca.* −1.8 V *vs.* Fc^{+}/Fc, likely corresponding to reduction of the ligand NO_2 groups based on comparison with the CV of the **H$_2$Sal^{NO2}** ligand and the similar reduction potential for 4-nitroanisole (Fig. S3, S4).[55] Similarly, **CrNSal^{H}** displays a quasi-reversible redox process at $E_{1/2}$ = 0.62 V and no other oxidation event was observed in the potential window (Fig. 2A). In contrast, the more electron-rich **CrNSal^{OMe}** and

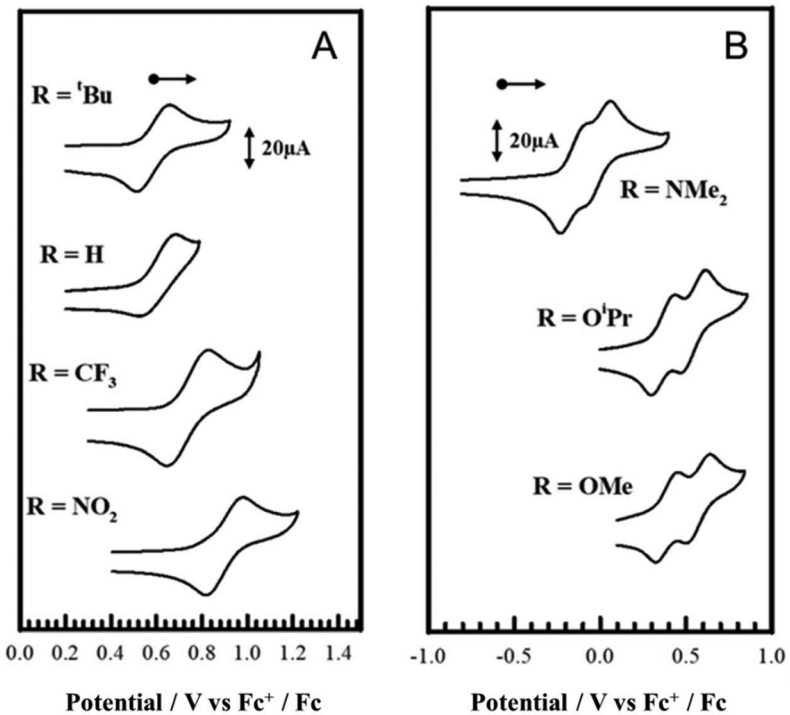

Fig. 2 Cyclic voltammograms of (A) **CrNSal^{tBu}**, **CrNSal^{H}**, **CrNSal^{CF3}** and **CrNSal^{NO2}**. (B) for **CrNSal^{NMe2}**, **CrNSal^{OiPr}** and **CrNSal^{OMe}**. Conditions: 0.1 M TBAP; CH_2Cl_2; 1 mM complex; T = 298 K; scan rate = 100 mV s^{-1}.

Table 1 Tabulated redox potentials for **CrNSal^{R}** *vs.* Fc^+/Fc[a] in volts.[b] Peak-to-peak separation in parentheses. Only the first two redox events (as applicable) are included

Compound	σ_p	$E_{pa}{}^1$	$E_{pc}{}^1$	$E_{1/2}{}^1$	$E_{pa}{}^2$	$E_{pc}{}^2$	$E_{1/2}{}^2$
CrNSal^{NO2}	0.78	0.83	0.99	0.91 (0.16)	—	—	—
CrNSal^{CF3} [b]	0.54	0.75	0.98	0.87 (0.23)	—	—	—
CrNSal^{H}	0.00	0.54	0.69	0.62 (0.15)	—	—	—
CrNSal^{tBu} [b]	−0.20	0.51	0.70	0.61 (0.19)	—	—	—
CrNSal^{OMe}	−0.27	0.34	0.46	0.40 (0.12)	0.53	0.65	0.59 (0.12)
CrNSal^{OiPr}	−0.45[c]	0.31	0.45	0.38 (0.14)	0.48	0.62	0.55 (0.14)
CrNSal^{NMe2} [b]	−0.83	0.12	0.05	−0.04 (0.17)	0.03	0.20	0.12 (0.17)

[a] Peak-to-peak separation for the Fc^+/Fc couple at 298 K in CH_2Cl_2 is 0.13 V. [b] Ref. 24. [c] The σ_p value for R = OiPr is suspected of being inaccurate (ref. 46), and in this case the σ_p^+ offers a better comparison: σ_p^+ = −0.83 (R = OMe); σ_p^+ = −0.85 (R = OiPr).

CrNSal^{OiPr} derivatives show two closely-spaced redox events (Fig. 2B and Table 1). Differential pulse voltammetry (DPV) was used to resolve these features, affording first and second redox potentials of $E_{1/2}$ = 0.40 and 0.59 V for **CrNSal^{OMe}**, and $E_{1/2}$ = 0.38 and 0.55 V for **CrNSal^{OiPr}**, respectively (Fig. S5).

The CV data for the **H_2Sal^{OMe}** and **H_2Sal^{OiPr}** ligands (Fig. S4) show two irreversible features upon oxidation. While the CV data supports that the R = O*i*Pr substituent is slightly more donating in comparison to R = OMe, the difference is smaller than expected based on the published σ_p values.[46] In this case, it is better to compare the corresponding σ_p^+ values, which account for substituents conjugated to the reaction center that can delocalize a positive charge.[46] The corresponding values (σ_p^+ = −0.83 for R = OMe); (σ_p^+ = −0.85 for R = O*i*Pr) better align with the electrochemistry data. Overall, the redox potentials reported for **CrNSal^{OMe}** and **CrNSal^{OiPr}** fall in between the redox potentials previously reported for **CrNSal^{tBu}** ($E_{1/2}$ = 0.61 V) and **CrNSal^{NMe2}** ($E_{1/2}$ = −0.04, 0.12 V),[24] and collectively illustrate the systematic modulation of the electronic structure enabled by the donating ability of the *para*-substituent on the salen scaffold. For both **CrNSal^{OMe}** and **CrNSal^{OiPr}**, the two quasi-reversible one-electron oxidation events are separated by ΔE_{ox} values of 0.20 V and 0.18 V as measured by DPV, respectively. These are slightly larger than that reported for **CrNSal^{NMe2}** (ΔE_{ox} = 0.16 V),[24] but overall the electrochemical data does not discern if the first oxidation is ligand-based or metal-based for either **CrNSal^{OMe}** or **CrNSal^{OiPr}**.[47,56] Further spectroscopic studies are therefore necessary to resolve the electronic structure of these oxidized species. In contrast, **CrNSal^{NO2}** and **CrNSal^{H}** each display a single oxidation event at $E_{1/2}$ = 0.91

V and 0.62 V *vs.* Fc^+/Fc, respectively, with no additional redox processes observed in the accessible potential window. Notably, the CV features for both complexes parallel those of previously reported **CrNSal^{CF3}** and **CrNSal^{tBu}**, as well as their Mn-analogues,[11] consistent with metal-based oxidation to form Cr(VI) complex for both R = H and NO_2 substituents.

2.4. UV-vis-NIR absorption spectroscopy

The UV-vis-NIR absorption spectra of the neutral **CrNSal^{R}** (R = NO_2, H, OMe, O*i*Pr) complexes are characteristic of square pyramidal Cr(V) d^1 species.[39,40] The four new derivatives exhibit a weak, low-energy band centered between 17 700–18 300 cm^{-1} (ε = 300–500 M^{-1} cm^{-1}), which is assigned to a metal centered d–d transition (Fig. 3 and Table 2).[39,40] In contrast, a more intense π–π* transition is observed at higher energies, the position of which shows a clear dependence on the electronic nature of the substituent (energy of π–π* transition NO_2 > H > OMe > O*i*Pr). Specifically, **CrNSal^{NO2}** displays the highest energy π–π* transition at 26 500 cm^{-1}, while **CrNSal^{OiPr}** exhibits the lowest at 24 700 cm^{-1}. These observations are consistent with the trend established in previously reported CF_3, *t*Bu, and NMe_2 analogues.[24]

Table 2 Key UV-Vis-NIR data for neutral and oxidized complexes. Conditions: 0.45 mM complex; *T* = 233 K; CH_2Cl_2

	$\lambda_{max}/10^3$ cm^{-1} ($e/10^3$ M^{-1} cm^{-1})	
Complex	Neutral	Mono-oxidized
CrNSal^{NO2}	26.5 (27.3), 18.3 (0.4)	23.0 (9.3), 11.4 (4.3)
CrNSal^{CF3} [a]	27.5 (8.1), 18.0 (0.3)	23.0 (5.8), 11.0 (2.2)
CrNSal^{H}	26.3 (6.4), 18.0 (0.3)	22.2 (6.6), 9.9 (2.5)
CrNSal^{tBu} [a]	25.5 (7.8), 18.0 (0.3)	21.9 (5.0), 8.1 (4.2)
CrNSal^{OMe}	24.6 (8.7), 17.9 (0.5)	24.2 (8.0), 7.0 (3.9)
CrNSal^{OiPr}	24.7 (8.2),17.7 (0.3)	23.9 (8.2), 7.3 (2.9)
CrNSal^{NMe2} [a]	23.3 (6.4)	21.3 (6.8), 18.8 (6.8), 11.5 (1.0)

[a] Ref. 24.

Next, based on the high oxidation potential of **CrNSal^{NO2}** ($E_{1/2}$ = 0.91 V *vs.* Fc^+/Fc), chemical oxidation was carried out using tris(2,4-dibromophenyl)aminium hexafluoroantimonate (magic green; $E_{1/2}$ = 1.1 V *vs.* Fc^+/Fc in CH_2Cl_2), which was an

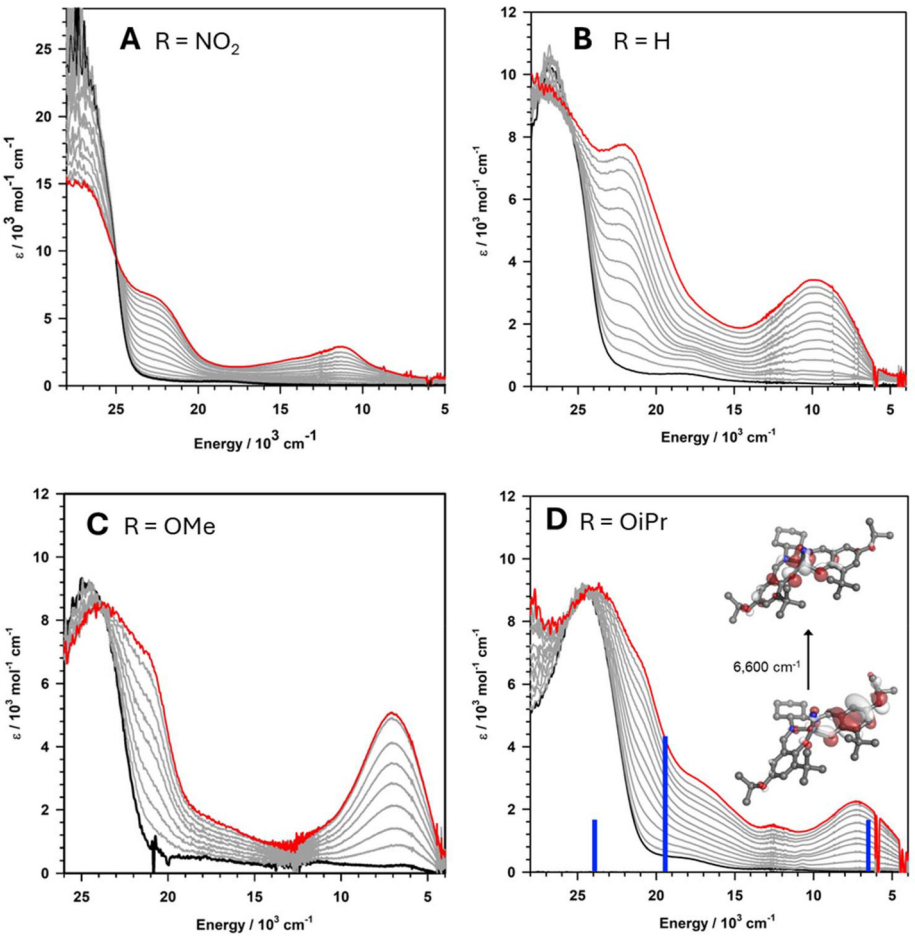

Fig. 3 Oxidation titrations monitored by UV-vis-NIR spectroscopy for (A) **CrNSal^{NO2}**, (B) **CrNSal^{H}**, (C) **CrNSal^{OMe}** and (D) **CrNSal^{OiPr}**. Black = neutral; grey = intermediate aliquots of oxidant; red = one equiv. of oxidant. Conditions: 0.45 mM complex; *T* = 233 K; CH_2Cl_2. For (D), the vertical blue lines indicate the most intense TD-DFT predicted bands for the singlet Cr(VI) electronic structure. In addition, the donor and acceptor orbitals for the predicted LMCT transition at 6700 cm^{-1} are shown.

effective chemical oxidant for all four derivatives (R = NO_2, H, OMe, OiPr).[57] Titration of one equiv. of oxidant into CH_2Cl_2 solutions of each neutral **CrNSal^{R}** complex at 233 K resulted in clean conversion to the oxidized species, as indicated by distinct isosbestic points (Fig. 3). For **[CrNSal^{NO2}]$^+$** and **[CrNSal^{H}]$^+$**, new absorptions are observed in the NIR and visible regions upon oxidation. Specifically, **[CrNSal^{NO2}]$^+$** exhibits transitions at 23 000 cm^{-1} (ε = 9.3 × 10^3 M^{-1} cm^{-1}) and 11 400 cm^{-1} (ε = 4.3 × 10^3 M^{-1} cm^{-1}), while **[CrNSal^{H}]$^+$** displays bands at 22 200 cm^{-1} (ε = 6.6 × 10^3 M^{-1} cm^{-1}) and 9900 cm^{-1} (ε = 2.5 × 10^3 M^{-1} cm^{-1}) (Fig. 3A, B and Table 2). The lower energy spectral features are fully consistent with ligand-to-metal charge transfer (LMCT) transitions,[11,17,24] and their energies align with those previously reported for **[Cr^{VI}NSal^{CF3}]$^+$** (11 000 cm^{-1}) and **[Cr^{VI}NSal^{tBu}]$^+$** (8100 cm^{-1}) (Table 2). The observed red-shift of LMCT bands across the NO_2 > CF_3 > H > *t*Bu series reflects the expected modulation of the ligand donor orbital energy in response to *para*-substituent effects. In combination with the electrochemical data, the UV-vis-NIR spectra support the assignment of metal-centered oxidation in **[CrNSal^{NO2}]$^+$** and **[CrNSal^{H}]$^+$**, affording Cr(VI) nitrido species.

We next turned to the alkoxy-substituted derivatives **CrNSal^{OMe}** and **CrNSal^{OiPr}** to assess whether their spectroscopic signatures might provide further insight into the electronic structure upon oxidation, given that their *para*-Hammett parameters lie intermediate between those of R = *t*Bu and R = NMe_2, which are known to promote metal-based and ligand-based oxidation, respectively. Upon one-electron oxidation of **CrNSal^{OMe}** and **CrNSal^{OiPr}**, clean isosbestic behavior was again observed, and broad transitions in the visible and NIR regions were evident (Fig. 3C and D).

[CrNSal^{OMe}]$^+$ displays new bands at 24 200 cm^{-1} (ε = 8.0 × 10^3 M^{-1} cm^{-1}) and 7000 cm^{-1} (ε = 3.9 × 10^3 M^{-1} cm^{-1}), while **[CrNSal^{OiPr}]$^+$** exhibits transitions at 23 900 cm^{-1} (ε = 8.2 × 10^3 M^{-1} cm^{-1}) and 7300 cm^{-1} (ε = 2.9 × 10^3 M^{-1} cm^{-1}) (Table 2). The lower energy bands follow the trend in LMCT energies discussed for **[Cr^{VI}NSal^{CF3}]$^+$** and **[Cr^{VI}NSal^{tBu}]$^+$**, and contrast sharply with the UV-vis-NIR spectra of the ligand-radical species **[Cr^{V}NSal^{NMe2}]$^{\bullet+}$**,[24] which exhibits an envelope of transitions between 21 000–15 000 cm^{-1} and a broader, lower-intensity NIR band at 11 500 cm^{-1} (ε = 1.0 × 10^3 M^{-1} cm^{-1}). Overall, the UV-vis-NIR spectral features for **[CrNSal^{OMe}]$^+$** and **[CrNSal^{OiPr}]$^+$**, supports metal-centered oxidation in both cases. The possibility of a temperature-dependent change in the locus of oxidation (valence tautomerism) was examined for the oxidized R = O*i*Pr derivative using UV-vis-NIR spectroscopy. Any shift in the locus of oxidation would be evident from distinct spectral signatures; however, across the temperature range studied (193–293 K), only minimal spectral variations were observed, indicating that the oxidation likely remains metal-centered (Fig. S6).[47,48,50,52] These results suggest that, despite the moderate electron-donating character of the R = OMe and R = O*i*Pr substituents, the locus of oxidation remains metal-centred, affording Cr(VI) nitrides with no significant electronic signatures characteristic of localized or delocalized ligand radicals observed.

2.5. Electronic paramagnetic resonance (EPR)

The X-band frozen solution EPR spectra of **CrNSal^{R}** (R = NO_2, H, OMe, O*i*Pr) are consistent with a Cr(V) $3d^1$ ($S = \frac{1}{2}$) ground state.[40] The spectra are well-resolved, showing distinct ^{53}Cr hyperfine coupling in both the parallel and perpendicular directions (Fig. 4). Simulation parameters reveal similar *g*-values across the series: $g_\perp$ = 1.994 and $g_\parallel$ = 1.951 for **CrNSal^{NO2}** and **CrNSal^{H}**; $g_\perp$ = 1.992 and $g_\parallel$ = 1.950 for **CrNSal^{OMe}** and **CrNSal^{OiPr}**. The ^{53}Cr hyperfine coupling constants ($A_\perp/A_\parallel$) also remain largely invariant, with $A_\perp$ ranging from 50–55 MHz and $A_\parallel$ held constant at 130 MHz across all four derivatives (Table 3).

To further probe the electronic structure of the oxidized **CrNSal^{R}** species, X-band EPR spectroscopy was performed on frozen CH_2Cl_2 solutions of **[CrNSal^{R}]$^+$** (R = NO_2, H, OMe, O*i*Pr) at 77 K. The neutral Cr(V) complexes exhibit uniaxial spectra consistent with an $S = \frac{1}{2}$ d^1 configuration, and therefore loss of EPR signal upon oxidation can be diagnostic of conversion to EPR-silent Cr(VI) (d^0, S = 0) or formation of strongly coupled ligand radical species.[58,59] Upon oxidation with 1 equiv. of magic green, both **[CrNSal^{NO2}]$^+$** and **[CrNSal^{H}]$^+$** exhibited significant loss of EPR signal intensity, retaining *ca.* 4% and *ca.* 18% of the original spin integration, respectively. Spectral simulations and inspection of the oxidized spectra confirmed that the residual signals in both cases are consistent with an axially symmetric Cr(V) species and most likely arise from unreacted Cr(V) complex. These data, in combination with the high redox potentials, absence of a second redox feature, and the UV-vis-NIR spectra, support metal-based oxidation to diamagnetic Cr(VI) species. Notably, the EPR behavior of these derivatives closely parallels that of previously reported **[CrNSal^{CF3}]$^+$** and **[CrNSal^{tBu}]$^+$**, reinforcing the assignment of metal-centered oxidation for the R = NO_2 and R = H derivatives.[24] Extending this analysis to the alkoxy-substituted derivatives, oxidation of **CrNSal^{OMe}** and **CrNSal^{OiPr}** also resulted in substantial attenuation of the Cr(V) EPR signal, with residual spin integrations of *ca.* 27% and *ca.* 15%, respectively. The residual signal is again consistent with an axially symmetric Cr(V) complex. While a 20% spin integration was reported for **[CrNSal^{NMe2}]$^{\bullet+}$**, the oxidized EPR spectrum was consistent with comproportionation resulting in both a Cr(V) signal and a bis-ligand radical signal associated with **[CrNSal^{NMe2}]$^{2+}$**.[24] The UV-vis-NIR spectra of **[CrNSal^{OMe}]$^+$** and **[CrNSal^{OiPr}]$^+$** lack the envelope of transitions between 24 000 cm^{-1} and 15 000 cm^{-1}, indicative of a localized phenoxyl radical species for **[CrNSal^{NMe2}]$^{\bullet+}$**. Taken together, these results support metal-centered oxidation to Cr(VI) for the alkoxy analogues. We attempted to further investigate the electronic structure of the **[CrNSal^{OiPr}]$^+$** complex using ^{1}H NMR, however, bulk oxidation at 0.1 M at 298 K resulted in a colour change and sample decomposition.

2.6. Solution infrared (IR) spectroscopy

To further investigate the locus of oxidation for **[CrNSal^{OMe}]$^+$** and **[CrNSal^{OiPr}]$^+$**, solution IR was employed to monitor

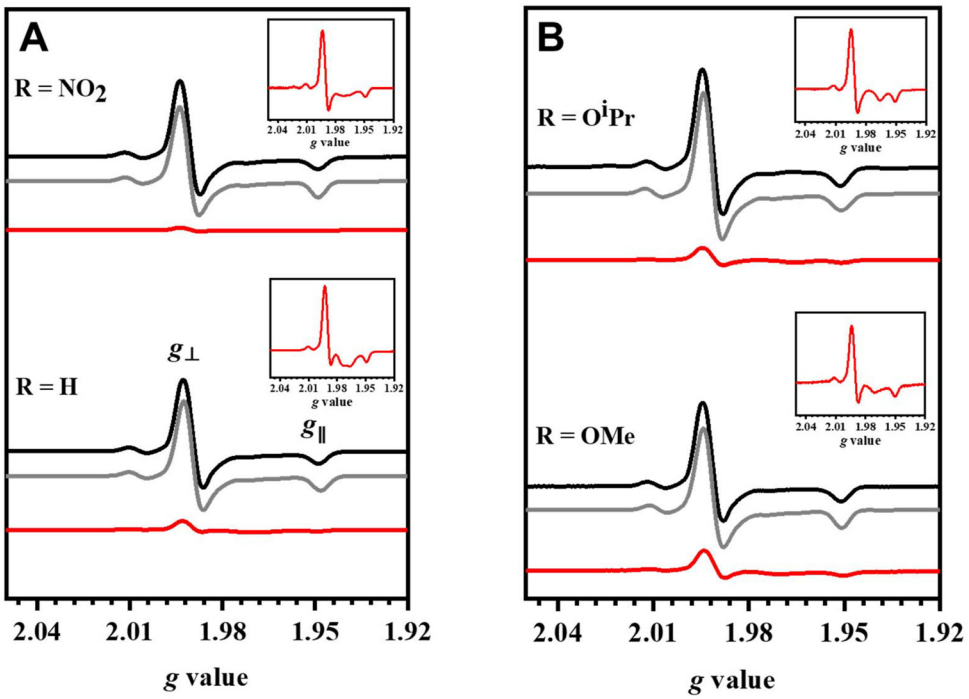

Fig. 4 Frozen solution EPR spectra for concentration-matched neutral **CrNSal^{R}** (black = experimental, grey = simulation) and mono-oxidized **[CrNSal^{R}]$^{+}$** (red = experimental). Conditions: T = 77 K; 0.45 mM complex; 0.1 M TBAP; Freq. = 9.4 GHz; Power = 2.0 mW; Mod. Amp. = 1 G (R = OMe), 3 G (R = NO_2, H), 6 G (R = O*i*Pr). Insets are the expanded view of the residual oxidized signal for mono-oxidized [CrNSal^{R}]$^{+}$.

Table 3 EPR simulation parameters for the four neutral complexes

Complex	$g_{\perp}$	A^{53Cr} (MHz)	$g_{\|\|}$	A^{53Cr} (MHz)
CrNSal^{NO2}	1.994	53	1.951	130
CrNSal^{H}	1.994	53	1.951	130
CrNSal^{O}M^{e}	1.992	50	1.950	130
CrNSal^{OiPr}	1.992	55	1.950	130

changes in the Cr≡N stretching frequency. For the neutral **CrNSal^{OiPr}**, a well-resolved band at 1014 cm^{-1} was attributed to ν(Cr≡N) (Fig. 5), consistent with the neutral Cr(v) state and comparable to the reported Cr≡N stretches for **CrNSal^{CF3}** (1029 cm^{-1}), **CrNSal^{tBu}** (1020 cm^{-1}), and **CrNSal^{NMe2}** (1020 cm^{-1}).[24,60] Upon oxidation to **[CrNSal^{OiPr}]$^{+}$**, the original Cr≡N band disappears, and two new bands emerge at 1041 and 1096 cm^{-1}. Although a definitive assignment of the Cr≡N stretch to one of these two bands cannot be made based on the current data, the clear shift to higher frequency upon oxidation strongly supports an increase in Cr≡N bond strength, consistent with conversion to a Cr(VI) (d^0) species. This can be attributed to a decrease in energy of the Cr d-orbitals upon oxidation from Cr(v) to Cr(VI) resulting in improved overlap with the nitride p-orbitals, and stronger bonding. For example, a *ca.* 80 cm^{-1} shift to 1096 cm^{-1} is similar to that observed for **[Cr^{VI}NSal^{tBu}]$^{+}$** ($\Delta\nu$ = +90 cm^{-1}),[24] and agrees with the DFT-calculated frequency shift ($\Delta\nu$ = +79 cm^{-1} for OiPr, *vide infra*). In contrast, ligand-based oxidation to **[Cr^{V}NSal^{NMe2}]$^{\cdot+}$** resulted in a negligible shift ($\Delta\nu$ = 1 cm^{-1}),[24] as expected for an oxidation

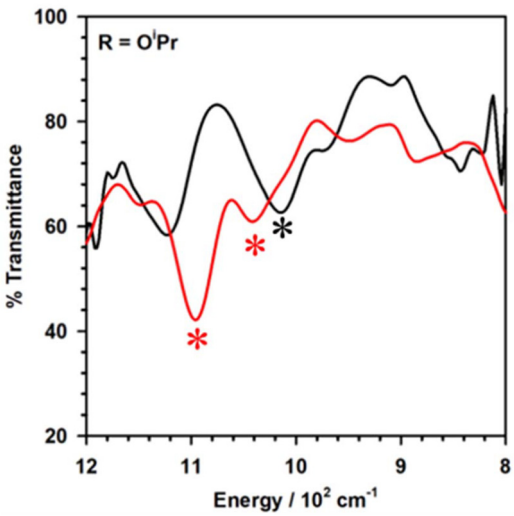

Fig. 5 Solution IR spectra for neutral (black) and chemically oxidized with magic green (red) for **CrNSal^{OiPr}**. **n*(Cr≡N). Conditions: 5 mM complex; T = 298 K; CH_2Cl_2.

event that does not perturb the metal–nitride core. For the **CrNSal^{OMe}** derivative, the Cr≡N stretch is less clearly resolved, likely manifest as a shoulder near 1020 cm^{-1}; however, following oxidation, new bands at 1041 and 1081 cm^{-1} are present, consistent with a shift to higher energy and again supportive of metal-based oxidation (Fig. S7). Taken together, the IR

spectra for the alkoxy-substituted derivatives, particularly of the R = OiPr analogue, align with the electrochemical, UV-vis-NIR, and EPR data in supporting the assignment of $[\mathbf{CrNSal}^{\mathbf{OMe}}]^+$ and $[\mathbf{CrNSal}^{\mathbf{O}i\mathbf{Pr}}]^+$ as Cr(VI) species.

2.7. Theoretical analysis

Density functional theory (DFT) calculations were employed to further understand the geometry and electronic structure of the neutral $\mathbf{CrNSal}^{\mathbf{R}}$ (R = NO_2, H, OMe, O*i*Pr) complexes. Geometry optimizations were performed using the UB3LYP/6-31G* level of theory with a polarizable continuum model (PCM) for CH_2Cl_2, a combination previously shown to yield good agreement with experimental metrical parameters.[24] The predicted bond lengths closely match the experimentally determined values, with all Cr–O, Cr–N(salen), and Cr≡N distances within ±0.04 Å of crystallographic data. The calculated Cr–N (nitride) distances range from 1.519–1.525 Å with the Cr center ~0.52 Å above the plane defined by the four donor atoms of the salen ligand, consistent with structural parameters obtained from X-ray crystallography. Spin density analysis on the neutral complexes reveals that the unpaired electron resides primarily on the Cr center with the singly occupied molecular orbital (SOMO) corresponding to the Cr d_{xy} orbital, which lies in the equatorial plane and is nonbonding with respect to the nitride ligand (Fig. 6, Fig. S8, and Table S3). This electronic structure is consistent with the experimentally confirmed Cr(V) (d^1) formulation.

To probe the electronic structures of the oxidized complexes $[\mathbf{CrNSal}^{\mathbf{R}}]^+$ (R = NO_2, H, OMe, O*i*Pr), geometry optimizations were performed for the singlet (Cr(VI), S = 0), broken-symmetry singlet (BSS, antiferromagnetically coupled Cr(V)-ligand radical, S = 0), and triplet (ferromagnetically coupled Cr(V)-ligand radical, S = 1) spin states. The computed relative energies are compiled in Table 4 (Tables S4–S6). The Cr(VI) singlet state is calculated to be the ground state for all four new derivatives. While electron-withdrawing (NO_2) and weakly donating (H) substituents predictably stabilize the Cr(VI) singlet, the same lowest-energy assignment persists even for electron-donating groups such as OMe and O*i*Pr. Notably, the energy gap between spin states narrows along the series NO_2 > H > OMe > O*i*Pr, consistent with increasing salen ligand electron-donating ability. The Cr(VI) singlet remains energetically favored over the BSS and triplet states even for $[\mathbf{CrNSal}^{\mathbf{O}i\mathbf{Pr}}]^+$, however, the BSS state lies only 0.3 kcal mol^{-1} higher in energy. Analysis of the computed Cr≡N stretching frequencies for the Cr(VI) singlet state solution for $[\mathbf{CrNSal}^{\mathbf{O}i\mathbf{Pr}}]^+$, obtained using the PCM(CH_2Cl_2) solvent model, predicts a shift to higher energy by 79 cm^{-1} relative to the neutral precursor, which aligns with the experimental solution IR data and further corroborates metal-based oxidation. In addition, time-dependent DFT (TD-DFT) calculations on the singlet Cr(VI) electronic structure affords the best match to the experimental UV-vis-NIR spectrum, with a predicted LMCT transition at 6700 cm^{-1} (Fig. 3D). Neither of the triplet or BSS Cr(V)-ligand radical electronic structures exhibit predicted bands below 16 000 cm^{-1} (see SI). Overall, the DFT-predicted metal-based oxidation for $[\mathbf{CrNSal}^{\mathbf{R}}]^+$ (R = NO_2, H, OMe, O*i*Pr) is consistent with experimental observations from CV, UV-vis-NIR spectroscopy, EPR, and solution-phase IR measurements.

Table 4 Predicted relative energies of different spin states for $[\mathbf{CrNSal}^{\mathbf{R}}]^+$ (kcal mol^{-1}). Computed using UBLYP/def2-TZVP/PCM (CH_2Cl_2) single-point calculations on geometries optimized at the UB3LYP/6-31G*/PCM(CH_2Cl_2) level

Complex	Singlet	BSS	Triplet
$[\mathbf{CrNSal}^{\mathbf{NO2}}]^+$	0	4.1	10.4
$[\mathbf{CrNSal}^{\mathbf{CF3}}]^+$	0	4.4	9.9
$[\mathbf{CrNSal}^{\mathbf{H}}]^+$	0	3.6	8.5
$[\mathbf{CrNSal}^{t\mathbf{Bu}}]^+$	0	2.8	6.4
$[\mathbf{CrNSal}^{\mathbf{OMe}}]^+$	0	1.9	2.3
$[\mathbf{CrNSal}^{\mathbf{O}i\mathbf{Pr}}]^+$	0	0.3	2.5
$[\mathbf{CrNSal}^{\mathbf{NMe2}}]^+$	2.3	0	0.6

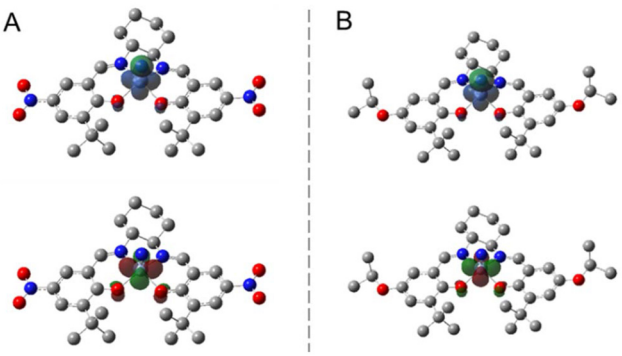

Fig. 6 Representative spin density (top) and SOMO (bottom) plots for (A) $\mathbf{CrNSal}^{\mathbf{NO2}}$ and (B) $\mathbf{CrNSal}^{\mathbf{O}i\mathbf{Pr}}$. R = H and R = OMe substituents exhibit similar plots (see Fig. S5).

2.8. Bis-oxidized $[\mathbf{CrNSal}^{\mathbf{O}i\mathbf{Pr}}]^{2+}$

Based on the presence of the second reversible redox process at relatively low potential ($E_{1/2}$ = 0.55 V *vs.* Fc^+/Fc) in the CV of $\mathbf{CrNSal}^{\mathbf{O}i\mathbf{Pr}}$ (Fig. 2B), we endeavoured to characterize the bis-oxidized complex $[\mathbf{CrNSal}^{\mathbf{O}i\mathbf{Pr}}]^{2+}$. We previously reported the bulk electrolysis of $\mathbf{CrNSal}^{\mathbf{NMe2}}$ to form $[\mathbf{CrNSal}^{\mathbf{NMe2}}]^{2+}$, which was characterized as a bis-radical species based on the observation of an isotropic EPR signal as a result of antiferromagnetic coupling of d^1 Cr(V) with one phenoxyl radical.[24] Unfortunately, bulk electrolysis of $\mathbf{CrNSal}^{\mathbf{O}i\mathbf{Pr}}$ resulted in sample decomposition, even for the mono-oxidized $[\mathbf{CrNSal}^{\mathbf{O}i\mathbf{Pr}}]^+$. We next investigated chemical oxidation using magic green ($E_{1/2}$ = 1.1 V *vs.* Fc^+/Fc in CH_2Cl_2), which afforded clean conversion from mono- to -bis-oxidized complex (Fig. 7). Spectral changes include loss of the low energy ligand-to-metal charge transfer (LMCT) transition at 7300 cm^{-1} (ε = 2.9 × 10^3 M^{-1} cm^{-1}), and the presence of a new band at 21 000 cm^{-1} (ε = 12.2 × 10^3 M^{-1} cm^{-1}); the new species is stable over a period of hours at 233 K. The spectrum for $[\mathbf{CrNSal}^{\mathbf{O}i\mathbf{Pr}}]^{2+}$ is similar to that previously reported for the doubly-oxidized Mn derivative $[\mathbf{MnNSal}^{\mathbf{O}i\mathbf{Pr}}]^{2+}$, which was characterized as a Mn(V) bis-ligand

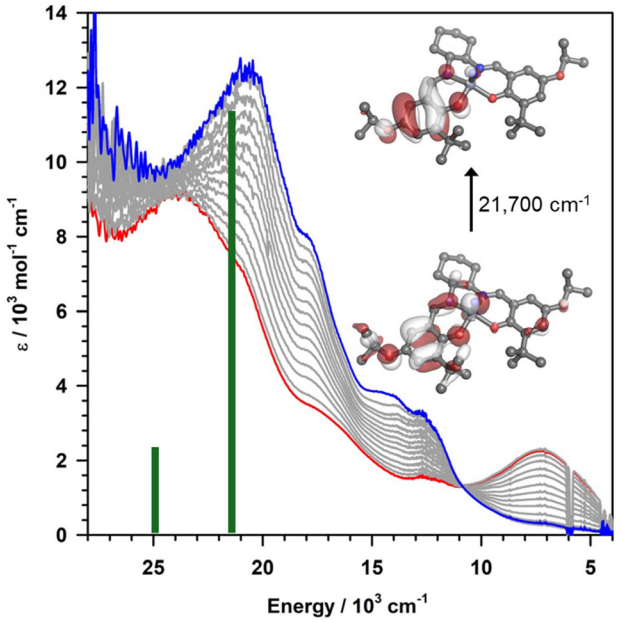

Fig. 7 Oxidation titration of $[\mathbf{CrNSal}^{\mathbf{OiPr}}]^{+}$ to $[\mathbf{CrNSal}^{\mathbf{OiPr}}]^{2+}$ monitored by UV-vis-NIR spectroscopy. Red = mono-oxidized; grey = intermediate aliquots of oxidant; blue = bis-oxidized. Conditions: 0.45 mM complex; T = 233 K; CH_2Cl_2. Vertical lines indicate the most intense TD-DFT predicted transitions for the doublet Cr(v) bis-phenoxyl complex electronic structure with the donor and acceptor orbitals corresponding to the predicted transition at 21 700 cm^{-1}.

radical species, resulting from reduction of Mn(vi) *via* the conversion of phenolate to phenoxyl upon bis-oxidation.[53] A similar metal-centered reduction upon one-electron oxidation has been observed for a Ni(ii) bis(phenoxyl) radical species.[61] Herein, the loss of the LMCT transition at 7300 cm^{-1}, and presence of the new band at 21 000 cm^{-1}, previously assigned as π→π* transition of coordinated phenoxyl radical,[62] are consistent with a Cr(v) bis(phenoxyl) radical species for $[\mathbf{CrNSal}^{\mathbf{OiPr}}]^{2+}$. An EPR spectrum of a sample of bis-oxidized $[\mathbf{CrNSal}^{\mathbf{OiPr}}]^{2+}$ in frozen CH_2Cl_2 (100 K) showed two essentially isotropic features (Fig. S9) at g = 2.006 and g = 1.971, with the latter broader signal consistent with a d^1 Cr(v) bis-phenoxyl radical electronic structure, in which one phenoxyl radical is antiferromagnetically-coupled with the d^1 Cr(v) center. The sharper signal at g = 2.006 is consistent with a free phenoxyl radical,[63,64] likely indicating partial decomposition of $[\mathbf{CrNSal}^{\mathbf{OiPr}}]^{2+}$ during sample transfer to an EPR tube for analysis. This result further reinforces the limited stability of $[\mathbf{CrNSal}^{\mathbf{OiPr}}]^{2+}$ in comparison to $[\mathbf{CrNSal}^{\mathbf{NMe2}}]^{2+}$, in line with the electrolysis experiment. Theoretical calculations on $[\mathbf{CrNSal}^{\mathbf{OiPr}}]^{2+}$ predict the doublet state (spin density, Fig. S10), a result of antiferromagnetic coupling of d^1 Cr(v) with one phenoxyl radical, to be of lowest energy, with the quartet state ~1.5 kcal mol^{-1} higher in energy. An initial guess for the Cr(vi) phenoxyl radical electronic structure results in collapse back to the predicted doublet state described above. This supports that the second oxidation results in reduction of Cr(vi) *via* the conversion of phenolate to phenoxyl, affording a d^1 Cr(v) bis-phenoxyl radical electronic structure for $[\mathbf{CrNSal}^{\mathbf{OiPr}}]^{2+}$. TD-DFT calculations on the antiferromagnetically coupled Cr (v) doublet electronic structure predict an intense transition at 21 700 cm^{-1} in line with the experimental spectrum, as well as the loss of the LMCT transition at low energy. While further characterization is needed, our current data supports that bis-oxidation of $\mathbf{CrNSal}^{\mathbf{OiPr}}$ results in a Cr(v) bis-phenoxyl complex.

3. Conclusion

This study expands the $\mathbf{CrNSal}^{\mathbf{R}}$ platform to now include NO_2, CF_3, H, *t*Bu, OMe, O*i*Pr and NMe_2 derivatives, enabling systematic investigation of how salen *para*-substituent electronics govern the oxidation locus in high-valent Cr complexes. While we hypothesized that alkoxy substituents might approach the redox threshold necessary for valence tautomerism, all experimental and computational data, including CV, UV-vis-NIR, EPR, solution IR, and DFT, consistently support metal-centered oxidation to Cr(vi) across the series. Despite narrowing singlet–BSS energy gaps for R = OMe and R = OiPr, no evidence of ligand radical character or redox delocalization was observed in the temperature range of 193–293 K, indicating that the locus of oxidation remains metal-based even for moderately donating substituents. Interestingly, bis-oxidation of $\mathbf{CrNSal}^{\mathbf{OiPr}}$ to form $[\mathbf{CrNSal}^{\mathbf{OiPr}}]^{2+}$ suggests metal-based reduction from Cr(vi) to afford a Cr(v) bis-phenoxyl radical species, such redox-induced electron rearrangement has been reported in other systems.[53,65–67] Additionally, the R = NO_2-substituted complex did not undergo Mn-like bimolecular nitride coupling at 233 K; however, spectroscopic and electrochemical signatures indicate enhanced nitride electrophilicity relative to the R = CF_3 analogue. Together, we find that the window for metal-based oxidation in Cr salen nitride complexes stretches further than expected, moving past R = *t*Bu to the more donating R = O*i*Pr and can be used to establish a foundation for designing tunable nitride transfer agents based on ancillary ligand electronic control.

4. Experimental

4.1. Materials and methods

All chemicals used were obtained from commercial suppliers and used without any further purification unless noted otherwise. All ligands and $\mathbf{MnNSal}^{\mathbf{H}}$ were synthesized according to literature procedures.[11,17,53] Dry tetrahydrofuran was obtained by refluxing over sodium in the presence of benzophenone under N_2. Dry CH_3CN was obtained by refluxing over calcium hydride under N_2. UV-vis-NIR data was collected on a Cary 5000 spectrophotometer equipped with custom designed immersion fiber-optic probes with a 1 mm path length. Constant temperatures were maintained with an FTS Multi-Cool Low Temperature Bath. ESI-MS was performed using an Agilent 6210 TOF ESI-MS system. Elemental analysis (C, H, N)

was performed at Simon Fraser University on a Carlo Erba EA1110 CHN elemental analyser. Evan's method ^{1}H NMR spectra was collected on a Bruker AVANCE III 500 MHz instrument. EPR spectra were collected on a Bruker EMXplus spectrometer operating with a premium X-band microwave bridge and HS resonator. Electrochemistry experiments were performed on PAR-263A potentiometer equipped with a silver wire reference electrode, a platinum disk counter electrode and glassy carbon working electrode under N_2 atmosphere. Electrolysis was performed with a Biologic SP300 potentiostat by using a carbon foam working electrode and was monitored by coulometry and rotating-disk electrode voltammetry. Solution IR spectra were collected on a PerkinElmer UTAR Two FT-IR spectrometer using a 1 mm Specac transmission cell.

4.2. Synthesis

4.2.1. Synthesis of CrNSal^{NO2}. Under a nitrogen atmosphere, 0.214 g (0.571 mmol) of $CrCl_3$·THF and 0.192 g (0.572 mmol) of **MnNSal^{H}** were dissolved in 2 mL of CH_3CN and stirred for 1 hour. 0.200 g (0.381 mmol) of **H$_2$Sal^{NO2}** was dissolved in 2 mL of 1 : 1 CH_2Cl_2/CH_3CN and 8 drops of NEt_3 and added dropwise to the [CrN] solution. After refluxing 1 hour, a precipitate formed, and the suspension was placed in a −20 °C freezer. The precipitate was collected by vacuum filtration and washed with 2 × 10 mL cold CH_3CN. **CrNSal^{NO2}** was isolated as a purple-brown solid. Yield 0.085 g (0.144 mmol, 38%). ESI-MS *m*/*z*: $\{M + H_2O + CH_3CN\}^-$ 647.23 100%. Anal. Cald (%) $C_{28}H_{34}CrN_5O_6$·0.5H_2O: C 56.28, H 5.90, N 11.72; Found (%): C 56.23, H 5.82, N 11.76. μ_{eff} = 1.86 (Evans method).

4.2.2. Synthesis of CrNSal^{H}. Under a nitrogen atmosphere, 0.259 g (0.691 mmol) of $CrCl_3$·THF and 0.231 g (0.689 mmol) of **MnNSal^{H}** were dissolved in 2 mL of CH_3CN and stirred for 1 hour. 0.200 g (0.460 mmol) of H_2Sal^H was dissolved in 2 mL of 1 : 1 CH_2Cl_2/CH_3CN and added dropwise to the [CrN] solution. After stirring 1 hour, a precipitate formed and 0.128 mL of NEt_3 was added. The suspension was stirred overnight, then concentrated *in vacuo*. The crude product was purified by column chromatography using CH_2Cl_2 as eluent (R_f = 0.7). **CrNSal^{H}** was isolated as a tan solid. Yield 0.050 g (0.100 mmol, 22%). ESI-MS *m*/*z*: 499.22 $\{M + H\}^+$ 100%. Anal. Calcd (%) $C_{28}H_{36}CrN_3O_2$: C 67.45, H 7.28, N 8.43; Found (%): C 67.32, H 7.35, N 8.21. μ_{eff} = 1.98 (Evans method).

4.2.3. Synthesis of CrNSal^{OMe}. To a yellow solution of 0.500 g **H$_2$Sal^{OMe}** (1.01 mmol) in 10 mL tetrahydrofuran was added 0.149 g $CrCl_2$ (1.212 mmol) and the reaction was stirred overnight under inert atmosphere. 30 mL of saturated ammonium chloride was added and stirred for 2 hours in air, followed by the addition of 25 mL of brine. The organic layer was dried over sodium sulfate, filtered and removed *in vacuo* to yield 0.500 g (0.862 mmol) of crude **CrClSal^{OMe}** intermediate. The intermediate was dissolved in 30 mL CH_2Cl_2 and 0.347 g of **MnNSal^{H}** (1.035 mmol) was added, refluxed for 1 hour, and the solvent was removed *in vacuo*. The crude product was purified by silica gel column chromatography using CH_2Cl_2 as the eluent (R_f = 0.4). **CrNSal^{OMe}** was isolated as a yellow-brown powder. Yield 0.209 g (0.374 mmol, 37%). ESI-MS *m*/*z*: 559.23 $\{M + H\}^+$ 100%. Anal. Calcd (%) $C_{30}H_{40}CrN_3O_4$: C 64.50, H 7.22, N 7.52; Found (%): 64.43, H 7.32, N 7.20. μ_{eff} = 1.71 (Evans method).

4.2.4. Synthesis of CrNSal^{OiPr}. To a yellow solution of 1.000 g **H$_2$Sal^{OiPr}** (1.82 mmol) in 20 mL tetrahydrofuran was added 0.268 g $CrCl_2$ (1.82 mmol) and the reaction was stirred overnight under inert atmosphere. 30 mL of saturated ammonium chloride was then added and stirred for 2 hours in air, followed by the addition of 25 mL of brine. The organic layer was dried over sodium sulfate, filtered, and removed *in vacuo* to yield 0.670 g (1.05 mmol) of crude **CrClSal^{OiPr}** intermediate. The intermediate was dissolved in 30 mL CH_2Cl_2 and 0.359 g of MnNSal^{H} (1.07 mmol) was added, refluxed for 1 hour, and the solvent was removed *in vacuo*. The crude product was purified by silica gel column chromatography using CH_2Cl_2 as the eluent (R_f = 0.3). **CrNSal^{OiPr}** was isolated as a yellow-brown powder. Yield 0.430 g (0.70 mmol, 38%). ESI-MS *m*/*z*: 615.31 $\{M + H\}^+$ 100%. Anal. Calcd (%) $C_{34}H_{48}CrN_3O_4$·0.5H_2O: C 65.47, H 7.92, N 6.74; Found (%):C 65.59, H 7.53, N 6.24. μ_{eff} = 2.04 (Evans method).

4.2.5. Synthesis of [CrNSal^{R}]$^+$. Oxidation titrations were performed by titration of 3.5 mL of 0.45 mM **CrNSal^{R}** with one equiv. of magic green oxidant in 20 μL additions at 253 K under a N_2 atmosphere. A solution of magic green was first standardized by titration with 3.5 mL of 0.45 mM NiSal^{tBu}, in which oxidant was slowly added until no further increase or a decrease in absorbance of the 4700 cm^{-1} band was observed. Excess oxidant will also manifest as a strong absorbance at 11 260 cm^{-1}. Frozen samples for EPR analysis were prepared as above in the presence of 0.1 M TBAP supporting electrolyte and stored in liquid N_2 for analysis.

4.3. X-Ray crystallography

All crystals were mounted on a 150 mm MiTeGen Dual-Thickness MicroMount using Paratone oil and measurements were made on a Bruker Photon II diffractometer with TRIUMPH-monochromated Mo Kα radiation (sealed tube) or Cu Kα radiation (Cu-micro source). The data were collected at a temperature of 298 K in a series of scans in 0.50° oscillations. Data were collected and integrated using the Bruker SAINT software package and were corrected for absorption effects using the multi-scan technique (SADABS) or (TWINABS).[68–71] All structures were solved by direct methods and refined using SIR97 and SIR92.[72,73] All non-hydrogen atoms were refined anisotropically. All hydrogen atoms were placed in calculated positions but not refined. All refinements were performed using the SHELXTL crystallographic software package of Bruker-AXS.[74] The molecular drawings were generated using POV and ORTEP.[75] CCDC 2496012–2496013, 2496015, and 2525742 contain the supplementary crystallographic data for this paper.

4.4. Theoretical analysis

All calculations were carried out using the Gaussian 16 program package (Revision A.03).[76] Geometry optimizations were performed with the UB3LYP functional and the 6-31G* basis set for all atoms.[77–79] This level of theory is shown to

provide good agreement with experimentally determined metrical parameters for Cr-salen systems.[24] Solvent effects were included through the polarizable continuum model (PCM) using CH_2Cl_2 (ε = 8.93) for all atoms.[80,81] Frequency calculations at the same level of theory confirmed that the optimized geometries correspond to minima on the potential energy surface. Single-point energy calculations were subsequently performed on the optimized geometries using the UBLYP functional and the TZVP basis set.[82,83] This local functional, which does not incorporate Hartree–Fock exchange, was shown to reproduce the experimentally observed Cr(VI) singlet ground state for the oxidized $[\mathbf{CrNSal^R}]^+$ complexes in our previous study. Additional single-point calculations using UM06L[84] and UMN15L[85] were conducted to assess the functional dependence of the spin-state energetics (Table S3). Geometry optimizations were also repeated at the UB3LYP-GD3/6-31G*/PCM(CH_2Cl_2) level to assess the influence of dispersion corrections;[86] however, for the present systems, inclusion or omission of dispersion does not produce any significant difference in the computed geometries or relative spin-state energies (Tables S4 and S5). TD-DFT calculations were performed on the optimized ground-state geometries of the mono- and bis-oxidized derivatives, considering all relevant spin states, using the ωB97X-D functional with the def2-TZVP basis set. The lowest 25 excited states were computed, and solvent effects of CH_2Cl_2 were included using the polarizable continuum model (PCM).

Conflicts of interest

There are no conflicts to declare.

Data availability

Supplementary information: full X-ray crystallographic details, additional electrochemistry and theoretical calculation data including the optimized metrical parameters. See DOI: https://doi.org/10.1039/d5dt02506k.

CCDC 2496012, 2496013, 2496015 and 2525742 contain the supplementary crystallographic data for this paper.[87a–d]

Acknowledgements

This work was supported by the Natural Sciences and Engineering Research Council (NSERC) Discovery Grants (RGPIN-2019-06749 and RGPAS-2019-00054 to T. S.) as well as NSERC Alliance Catalyst (ALLRP-587326-23). The Digital Research Alliance of Canada is thanked for access to computational resources. W. V. thanks NSERC for a postgraduate fellowship. S. M. thanks Mitacs for a Globalink Graduate Fellowship (GLF599). G. A. M. acknowledges NSERC for a postgraduate fellowship. M. U. D-J. thanks the ministry of science and technology in Mexico (SECIHTI) for funding through the supercomputing national laboratory facility (LNS).

References

1 M. N. Cosio and D. C. Powers, *Nat. Rev. Chem.*, 2023, **7**, 424–438.
2 T. Schmidt-Räntsch, H. Verplancke, J. N. Lienert, S. Demeshko, M. Otte, G. P. van Trieste, K. A. Reid, J. H. Reibenspies, D. C. Powers, M. C. Holthausen and S. Schneider, *Angew. Chem., Int. Ed.*, 2022, **61**, e202115626.
3 N. P. van Leest, J. I. van der Vlugt and B. de Bruin, in *Redox-Active Ligands*, Wiley, 2024, pp. 21–52.
4 C. Schiller, D. Sieh, N. Lindenmaier, M. Stephan, N. Junker, E. Reijerse, A. A. Granovsky and P. Burger, *J. Am. Chem. Soc.*, 2023, **145**, 11392–11401.
5 J. Oh, S.-L. Zheng, K. M. Carsch, T. P. Latendresse, C. E. Casaday, B. M. Campbell and T. A. Betley, *J. Am. Chem. Soc.*, 2025, **147**, 3174–3184.
6 S. Mahato, O. Castro-Sandoval, V. Cheung, R. M. Clarke, S. Kamal, L. Kaake, O. Jarjayes, F. Thomas and T. Storr, *J. Am. Chem. Soc.*, 2025, **147**, 37299–37305.
7 C. C. Almquist, T. Rajeshkumar, W. Zhou, L. Maron and W. E. Piers, *J. Am. Chem. Soc.*, 2025, **147**, 40374–40388.
8 R. A. Eikey and M. M. Abu-Omar, *Coord. Chem. Rev.*, 2003, **243**, 83–124.
9 J. M. Smith, *Prog. Inorg. Chem.*, 2014, **59**, 417–470.
10 J. F. Berry, *Comments Inorg. Chem.*, 2009, **30**, 28–66.
11 R. M. Clarke and T. Storr, *J. Am. Chem. Soc.*, 2016, **138**, 15299–15302.
12 A. G. Maestri, K. S. Cherry, J. J. Toboni and S. N. Brown, *J. Am. Chem. Soc.*, 2001, **123**, 7459–7460.
13 T. J. Crevier, B. K. Bennett, J. D. Soper, J. A. Bowman, A. Dehestani, D. A. Hrovat, S. Lovell, W. Kaminsky and J. M. Mayer, *J. Am. Chem. Soc.*, 2001, **123**, 1059–1071.
14 T. J. Meyer and M. H. V. Huynh, *Inorg. Chem.*, 2003, **42**, 8140–8160.
15 W.-L. Man, W. W. Y. Lam, H.-K. Kwong, S.-M. Yiu and T.-C. Lau, *Angew. Chem., Int. Ed.*, 2012, **51**, 9101–9104.
16 E. M. Zolnhofer, M. Käß, M. M. Khusniyarov, F. W. Heinemann, L. Maron, M. van Gastel, E. Bill and K. Meyer, *J. Am. Chem. Soc.*, 2014, **136**, 15072–15078.
17 S. Mahato, W. VandeVen, G. A. MacNeil, J. M. Pulfer and T. Storr, *Chem. Sci.*, 2024, **15**, 2211–2220.
18 W.-L. Man, J. Xie, P.-K. Lo, W. W. Lam, S.-M. Yiu, K.-C. Lau and T.-C. Lau, *Angew. Chem., Int. Ed.*, 2014, **53**, 8463–8466.
19 J. Schoffel, A. Y. Rogachev, S. DeBeer George and P. Burger, *Angew. Chem., Int. Ed.*, 2009, **48**, 4734–4738.
20 R. Thompson, B. L. Tran, S. Ghosh, C. H. Chen, M. Pink, X. Gao, P. J. Carroll, M.-H. Baik and D. J. Mindiola, *Inorg. Chem.*, 2015, **54**, 3068–3077.
21 L. N. Grant, M. Bhunia, B. Pinter, C. Rebreyend, M. E. Carroll, P. J. Carroll, B. de Bruin and D. J. Mindiola, *Inorg. Chem.*, 2021, **60**, 5635–5646.
22 L. N. Grant, B. Pinter, T. Kurogi, M. E. Carroll, G. Wu, B. C. Manor, P. J. Carroll and D. J. Mindiola, *Chem. Sci.*, 2017, **8**, 1209–1224.
23 L. N. Grant, B. Pinter, J. Gu and D. J. Mindiola, *J. Am. Chem. Soc.*, 2018, **140**, 17399–17403.

24 D. Martelino, S. Mahato, W. VandeVen, N. M. Hein, R. M. Clarke, G. A. MacNeil, F. Thomas and T. Storr, *J. Am. Chem. Soc.*, 2022, **144**, 11594–11607.
25 H. Shi, H. K. Lee, Y. Pan, K.-C. Lau, S.-M. Yiu, W. W. Y. Lam, W.-L. Man and T.-C. Lau, *J. Am. Chem. Soc.*, 2021, **143**, 15863–15872.
26 F. S. Schendzielorz, M. Finger, C. Volkmann, C. Würtele and S. Schneider, *Angew. Chem., Int. Ed.*, 2016, **55**, 11417–11420.
27 D. Sieh and P. Burger, *J. Am. Chem. Soc.*, 2013, **135**, 3971–3982.
28 G. P. Connor, B. Q. Mercado, H. M. C. Lant, J. M. Mayer and P. L. Holland, *Inorg. Chem.*, 2019, **58**, 10791–10801.
29 N. G. Léonard, T. Chantarojsiri, J. W. Ziller and J. Y. Yang, *J. Am. Chem. Soc.*, 2022, **144**, 1503–1508.
30 J. J. Scepaniak, J. A. Young, R. P. Bontchev and J. M. Smith, *Angew. Chem.*, 2009, **121**, 3204–3206.
31 J. Chatt, J. R. Dilworth and R. L. Richards, *J. Chem. Soc., Dalton Trans.*, 1977, 1852–1860.
32 M. Keener, M. Peterson, R. Hernández Sánchez, V. F. Oswald, G. Wu and G. Ménard, *Chem. – Eur. J.*, 2017, **23**, 11479–11484.
33 G. B. Panetti, J. Kim, M. S. Myong, M. J. Bird, G. D. Scholes and P. J. Chirik, *J. Am. Chem. Soc.*, 2024, **146**, 27610–27621.
34 D. Wang, F. Loose, P. J. Chirik and R. R. Knowles, *J. Am. Chem. Soc.*, 2019, **141**, 4795–4799.
35 S. Kim, H. Y. Zhong, Y. Park, F. Loose and P. J. Chirik, *J. Am. Chem. Soc.*, 2020, **142**, 9518–9524.
36 L. E. Martinez, J. L. Leighton, D. H. Carsten and E. N. Jacobsen, *J. Am. Chem. Soc.*, 1995, **117**, 5897–5898.
37 D. J. Darensbourg, J. C. Yarbrough, C. Ortiz and C. C. Fang, *J. Am. Chem. Soc.*, 2003, **125**, 7586–7591.
38 Y. Nieves-Quinones, T. J. Paniak, Y. E. Lee, S. M. Kim, S. Tcyrulnikov and M. C. Kozlowski, *J. Am. Chem. Soc.*, 2019, **141**, 10016–10032.
39 J. Bendix, *J. Am. Chem. Soc.*, 2003, **125**, 13348–13349.
40 K. Meyer, J. Bendix, E. Bill, T. Weyhermüller and K. Wieghardt, *Inorg. Chem.*, 1998, **37**, 5180–5188.
41 B. S. Billow, R. D. Bemowski, S. A. DiFranco, R. J. Staples and A. L. Odom, *Organometallics*, 2015, **34**, 4567–4573.
42 D. J. Mindiola and C. C. Cummins, *Angew. Chem., Int. Ed.*, 1998, **37**, 945–947.
43 G. Golubkov and Z. Gross, *Angew. Chem., Int. Ed.*, 2003, **42**, 4507–4510.
44 J. Bendix, C. Anthon, M. Schau-Magnussen, T. Brock-Nannestad, J. Vibenholt, M. Rehman and S. P. A. Sauer, *Angew. Chem., Int. Ed.*, 2011, **50**, 4480–4483.
45 T. Birk and J. Bendix, *Inorg. Chem.*, 2003, **42**, 7608–7615.
46 C. Hansch, A. Leo and R. W. Taft, *Chem. Rev.*, 1991, **91**, 165–195.
47 T. Storr, P. Verma, R. C. Pratt, E. C. Wasinger, Y. Shimazaki and T. D. P. Stack, *J. Am. Chem. Soc.*, 2008, **130**, 15448–15459.
48 D. N. Hendrickson and C. G. Pierpont, in *Spin Crossover in Transition Metal Compounds II*, Springer, 2004, pp. 63–95.
49 J. Rall, M. Wanner, M. Albrecht, F. M. Hornung and W. Kaim, *Chem. – Eur. J.*, 1999, **5**, 2802–2809.
50 C. Metzger, R. Dolai, S. Reh, H. Kelm, M. Schmitz, B. Oelkers, M. Sawall, K. Neymeyr and H.-J. Krüger, *Chem. – Eur. J.*, 2023, **29**, e202300091.
51 H. Ohtsu and K. Tanaka, *Angew. Chem., Int. Ed.*, 2004, **43**, 6301–6303.
52 N. G. R. Hearns, J. L. Korčok, M. M. Paquette and K. E. Preuss, *Inorg. Chem.*, 2006, **45**, 8817–8819.
53 N. M. Hein, G. A. MacNeil and T. Storr, *Inorg. Chem.*, 2021, **60**, 16895–16905.
54 L. A. Bottomley and F. L. Neely, *Inorg. Chem.*, 1997, **36**, 5435–5439.
55 A. Kuhn, K. G. von Eschwege and J. Conradie, *J. Phys. Org. Chem.*, 2012, **25**, 58–68.
56 L. Chiang, A. Kochem, O. Jarjayes, T. J. Dunn, H. Vezin, M. Sakaguchi, T. Ogura, M. Orio, Y. Shimazaki and F. Thomas, *Chem. – Eur. J.*, 2012, **18**, 14117–14127.
57 N. G. Connelly and W. E. Geiger, *Chem. Rev.*, 1996, **96**, 877–910.
58 M. Orio, O. Jarjayes, H. Kanso, C. Philouze, F. Neese and F. Thomas, *Angew. Chem., Int. Ed.*, 2010, **49**, 4989–4992.
59 A. Dei, D. Gatteschi, L. Pardi, A. L. Barra and L. C. Brunel, *Chem. Phys. Lett.*, 1990, **175**, 589–592.
60 E. D. Hedegaard, M. Schau-Magnussen and J. Bendix, *Inorg. Chem. Commun.*, 2011, **14**, 719–721.
61 M. Kawai, T. Yamaguchi, S. Masaoka, F. Tani, T. Kohzuma, L. Chiang, T. Storr, K. Mieda, T. Ogura, R. K. Szilagyi and Y. Shimazaki, *Inorg. Chem.*, 2014, **53**, 10195–10202.
62 T. Kurahashi and H. Fujii, *J. Am. Chem. Soc.*, 2011, **133**, 8307–8316.
63 S. Itoh, S. Takayama, R. Arakawa, A. Furuta, M. Komatsu, A. Ishida, S. Takamuku and S. Fukuzumi, *Inorg. Chem.*, 1997, **36**, 1407–1416.
64 R. Hicks, *Stable Radicals*, Wiley, 2011.
65 Y. Shimazaki, T. D. P. Stack and T. Storr, *Inorg. Chem.*, 2009, **48**, 8383–8392.
66 S. A. DiFranco, B. S. Billow, R. D. Bemowski and A. L. Odom, *J. Am. Chem. Soc.*, 2007, **129**, 8210–8211.
67 L. Lohmeyer, F. Schön, E. Kaifer and H.-J. Himmel, *Angew. Chem., Int. Ed.*, 2021, **60**, 10415–10422.
68 *SADABS*, Bruker AXS Inc., Madison, WI, 2003.
69 *TWINABS*, Bruker AXS Inc., Madison, WI, 2007.
70 *TWINABS*, Bruker AXS Inc., Madison, WI, 2008.
71 *SAINT*, Bruker AXS Inc., Madison, WI, 1997.
72 A. Altomare, M. C. Burla, M. Camalli, G. L. Cascarano, C. Giacovazzo, A. Guagliardi, A. G. G. Moliterni, G. Polidori and R. Spagna, *J. Appl. Crystallogr.*, 1999, **32**, 115–119.
73 A. Altomare, G. Cascarano, C. Giacovazzo and A. Guagliardi, *J. Appl. Crystallogr.*, 1993, **26**, 343–350.
74 *SHELXTL*, Bruker AXS Inc., Madison, WI, 1997.
75 L. J. Farrugia, *J. Appl. Crystallogr.*, 1997, **30**, 565.
76 M. J. Frisch, *et al.*, *Gaussian 16*, Gaussian Inc., Wallingford, CT, 2016.
77 A. D. Becke, *J. Chem. Phys.*, 1993, **98**, 5648–5652.
78 P. J. Stephens, F. J. Devlin, C. F. Chabalowski and M. J. Frisch, *J. Phys. Chem.*, 1994, **98**, 11623–11627.

79 R. Krishnan, J. S. Binkley, R. Seeger and J. A. Pople, *J. Chem. Phys.*, 1980, **72**, 650–654.
80 V. Barone, M. Cossi and J. Tomasi, *J. Comput. Chem.*, 1998, **19**, 404–417.
81 J. Tomasi, B. Mennucci and E. Cancès, *J. Mol. Struct. (THEOCHEM)*, 1999, **464**, 211–226.
82 A. Schäfer, H. Horn and R. Ahlrichs, *J. Chem. Phys.*, 1992, **97**, 2571–2577.
83 A. Schäfer, C. Huber and R. Ahlrichs, *J. Chem. Phys.*, 1994, **100**, 5829–5835.
84 Y. Zhao and D. G. Truhlar, *Theor. Chem. Acc.*, 2008, **120**, 215–241.
85 H. S. Yu, X. He, S. L. Li and D. G. Truhlar, *Chem. Sci.*, 2016, **7**, 5032–5051.
86 S. Grimme, J. Antony, S. Ehrlich and H. Krieg, *J. Chem. Phys.*, 2010, **132**, 154104.
87 (*a*) CCDC 2496012: Experimental Crystal Structure Determination, 2026, DOI: 10.5517/ccdc.csd.cc2ps9jb; (*b*) CCDC 2496013: Experimental Crystal Structure Determination, 2026, DOI: 10.5517/ccdc.csd.cc2ps9kc; (*c*) CCDC 2496015: Experimental Crystal Structure Determination, 2026, DOI: 10.5517/ccdc.csd.cc2ps9mf; (*d*) CCDC 2525742: Experimental Crystal Structure Determination, 2026, DOI: 10.5517/ccdc.csd.cc2qs7kb.